Available online at www.sciencedirect.com

jmr&t Journal of Materials Research and Technology

journal homepage: www.elsevier.com/locate/jmrt

Achieving high strength and ductility in Fe–Mn–Al–C austenitic steel via vanadium microalloying and aging

Guofeng Zhang [a], *Suotao Wang* [a], *Bo Li* [a], *Bohan Chen* [a,c], *Bing Zhang* [a,b,**], *Xingyu Zhang* [a], *Mingzhen Ma* [a], *Riping Liu* [a,*]

[a] *State Key Laboratory of Metastable Materials Science and Technology, Yanshan University, Qinhuangdao 066004, China*

[b] *Key Laboratory of New Processing Technology for Nonferrous Metal & Materials, Ministry of Education, Guilin University of Technology, Guilin 511004, China*

[c] *Department of Mechanical Engineering, The Hong Kong Polytechnic University, Hong Kong*

ARTICLE INFO

Article history:
Received 1 March 2023
Accepted 9 May 2023
Available online 11 May 2023

Keywords:
V addition
Microstructure evolution
Mechanical properties
κ-Carbide

ABSTRACT

An investigation was performed to evaluate the effect of vanadium (V) addition on the microstructure and the tensile behavior of Fe–27Mn–8Al-1.0C austenite lightweight steel after annealing and subsequently aging. The grain size of austenite in V-added steels was effectively refined and many nano-sized VC particles were observed in the austenite grains, compared to V-free steels, under annealed conditions. Subsequent aging promotes the precipitation of κ-carbide from the austenite matrix, and the dual-nanoprecipitation consisting of nano-sized VC and κ-carbide particles further improves the strength of the steel. Because of this, the current steels have good ductility (up to 41% total elongation) even when aged and high yield and ultimate tensile strengths of up to 1009 MPa and 1243 MPa, respectively. By examining the dislocation structure of the specimens during deformation, it was also possible to determine how precipitates affected the rate of strain hardening. As a result, the strain hardening rate of the V-added steel after aging is effectively improved at the initial deformation by the precipitation of VC particles, which compensates for the decrease in strain hardening rate due to shearable κ-carbide. This study provides a strategy to obtain an excellent combination of strength and ductility in lightweight steel by V microalloying and simple thermomechanical treatment.

1. Introduction

The current challenge for automotive steel is to meet fuel economy, formability, crashworthiness, and safety. High manganese austenitic lightweight steels (HMns) are well suited to meet the requirements for automotive steels because they combine excellent tensile strength and ductility with a low density [1–8]. These steels have high manganese (18–32 wt%) and carbon content (0.6–2.0 wt%), making the

* Corresponding author.
** Corresponding author.
E-mail addresses: zhangbing@ysu.edu.cn (B. Zhang), riping@ysu.edu.cn (R. Liu).

https://doi.org/10.1016/j.jmrt.2023.05.090

austenite stable to form a continuous austenitic matrix [9–13]. This allows higher aluminum content (up to 12 wt%) to be added to the steel, as the addition of lighter aluminum elements can significantly reduce the density, each additional 1 wt% of Al content results in a 1.3% decrease in density of steel [3,8,14,15].

The high aluminum and carbon content in HMns steels promotes the formation of κ-carbide, an $L'1_2$ ordered phase, with the ideal stoichiometry of $(Fe,Mn)_3AlC$ [16–18]. According to reports, the spinodal decomposition during quenching after solution treatment or aging at 450 °C-700 °C causes κ-carbide precipitates from the austenite matrix. κ-Carbide uniformly distribute in the austenite matrix, maintaining a coherent interface with the austenitic matrix due to the lower lattice mismatch [19–21]. The strategy of κ-carbide precipitation strengthening in lightweight steels to improve the strength of the material has been widely investigated recently. Usually, this nanoscale carbide precipitates in the austenite matrix during the lightweight steel undergoes aging treatment. It maintains a coherent interface with the austenite, thus improving the material's tensile strength while causing less damage to the ductility [1,20,22,23]. However, there is an upper limit to the maximum value of material strength improvement with κ-carbide precipitation strengthening. With increasing aging time, κ-carbide coarsens rapidly, and intergranular κ-carbide (up to several μm) precipitates at the austenite grain boundaries, resulting in no further increase in material strength and fatal damage to ductility [22,24]. Furthermore, the strain hardening rate of the age-strengthened lightweight steel is reduced because the nanoscale κ-carbide particles can be cut through by slip dislocations during deformation [24–26]. It is difficult to achieve the desired strength-ductility balance of the material using κ-carbide precipitation strengthening alone.

Thus, a multi-strategy must be used to achieve the desired strength and ductility. For example, to refine the austenite grains and thus achieve grain boundary strengthening, cold-rolled steel plates undergo recovery and recrystallization annealing heat treatment [27,28]. However, the short annealing time poses a challenge for industrial production. In addition, the B2 phase was introduced in some previous studies to improve the strength of steel by adding Ni and Cu; however, controlling the distribution and size of the B2 phase to damage the ductility is difficult [29,30]. Microalloying effectively improves the mechanical properties of HMn steel. Studies have shown that adding some microalloying elements improve the microstructure and mechanical properties of HMn steels [3]. For example, the addition of Mo introduces MC-type carbides to improve the strength of the steel, thereby inhibiting the precipitation of κ-carbides [9]. Moreover, the addition of Si promotes the coarseness of κ-carbides [31]. Other alloying elements, such as Ti, Nb, and V, have been used to improve the yield strength (YS) and work hardening by precipitation hardening of nano-sized precipitates (Ti, Nb, V)C. Furthermore, related methods have been widely used to enhance the YS of ferritic, pearlitic, martensitic, and bainitic steels with a body-centered cubic (BCC) structure. Compared to Ti or Nb microalloying, the V microalloying precipitated phase can be redissolved during reheating [32]. Fine VC precipitates were introduced into austenitic twinning-induced plasticity steel, and the results showed that YS was enhanced by 100 MPa through precipitation strengthening and grain refinement strengthening. However, V-alloyed HMn steels were rarely been investigated, and the precipitation behavior of VC and its effect on the microstructure and mechanical properties of austenitic lightweight steels remained inadequate [33].

In this study, V-alloyed austenitic lightweight steels were subjected to a two-step heat treatment (annealing and subsequent aging) to promote the precipitation of VC and κ-carbide, thereby effectively achieving the optimal combination of YS and ductility of austenitic lightweight steels. The interaction between the two precipitated phases and their effects on the microstructure of austenitic before and after deformation were systematically investigated. This study aimed to provide a strategy to improve the yield strength and to regulate the microstructure of austenitic lightweight steels.

2. Experimental

2.1. Materials preparation and processing

The examined steel had a nominal composition Fe–27Mn–8Al-1.0C-(0,0.5) V. A 50 kg ingot was prepared in a vacuum induction melting furnace under an argon atmosphere. It has a density of 6.72 g cm^{-3} determined using Archimedes' principle, which is 14.6% lower than pure Fe (7.87 g cm^{-3}). The ingots were forged into round bars of φ60 mm at 1140 °C and air-cooled to room temperature. Next, electric discharge wire cutting was used to produce a 60 × 20 × 20 mm square at 1200 °C for 2 h. The experimental steel was then hot-rolled into 3 mm plates (total deformation of 85%) in the temperature range of 950 °C-1050 °C, and water was quenched to room temperature. The hot-rolled plate was cold-rolled to 1.2 mm at room temperature. The cold-rolled plate was annealed at 900 °C for 3 min and water cooled to room temperature. Finally, the annealed specimens were aged at 600 °C, held for 120 min, and then water cooled to room temperature. Thermo-Calc phase diagram calculation software was used to determine the annealing and aging temperatures, as shown in Fig. 1. Following, annealed and aged V-free are abbreviated as A90 and AG60, whereas annealed and aged V-added steels are abbreviated as VA90 and VAG60, respectively.

2.2. Sample preparation and characterization

The microstructures of the samples were analyzed by X-ray diffraction (XRD, Rigaku D/max-2500/PC), scanning electron microscopy (SEM, Zeiss GEMINI 460, Field Emission Gun), electron backscattered diffraction (EBSD, EDAX Velocity) and transmission electron microscopy (TEM, FEI Talos F200x). XRD was used to determine the phase structure of the samples, with Cu Kα radiation, in the middle part of the RD-TD plane. The scan step was 0.02° with a scanning time of 2 s. After the specimens (perpendicular to TD) were electrolytically polished at −20 °C at 20 V, EBSD was performed at an accelerating voltage of 20 kV with a scan step of 0.15 μm. EBSD data were analyzed using TSL OIM analysis 8 software. TEM specimens were prepared in 90% ethanol +10% perchloric acid solution in

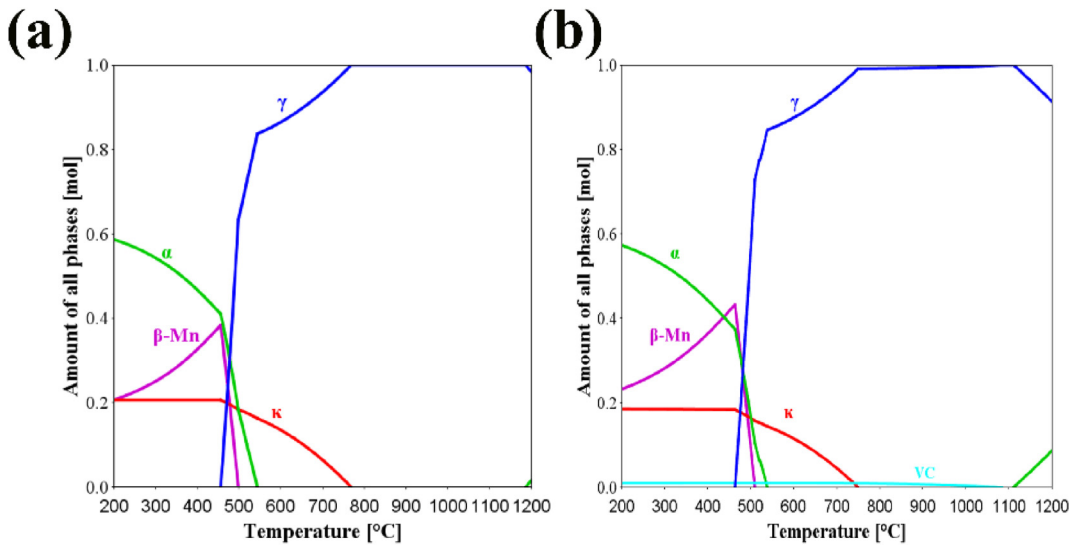

Fig. 1 – Phase diagram calculated by Thermo-Calc software of (a) V-free steel and (b) V-added steel.

a twin-jet electrochemical polishing process at 28 V and −25 °C.

Dog-bone-shaped tensile samples (gauge geometry: 20 mm × 4 mm × 1.2 mm) were machined by electrical discharge machining parallel to the rolling direction (RD). Three tensile samples were tested for each heat treatment condition. Uniaxial tensile tests (ASTM: E8/E8M-16a) were performed at room temperature on an Instron 5982 testing machine, and the strain was measured with an extensometer at an initial strain rate of 5×10^{-4} s^{-1}. The microhardness of specimens was measured using FM-ARS9000 Vickers hardness with a load of 500 gf, taking 20 points per specimen.

3. Result

3.1. Microstructural characterization

Based on Thermo-Calc results, Fig. 1 showed a slight decrease in the volume fraction of austenite and κ-carbide due to the addition of V. Fig. 2 shows XRD patterns of the as-annealed and as-aged 0V and 0.5V steel. The diffraction peaks of γ-austenite were identified in all the samples. Note that the nanoscale κ-carbide and VC precipitate have hardly been shown due to the small volume fraction and fine size. Fig. 3a–d shows EBSD inverse pole figure (IPF) maps of the A90, VA90, AG60, and VAG60 steels and the annealed twins are marked with black arrows. The grain size of steels is calculated using EBSD analysis, as is shown in Fig. 4. The microstructure of annealed 0V-steel consists of equiaxed austenite with a grain size of about 9.9 μm. The grain size of the 0.5V steel underwent significant refinement as compared with the V-free steel, with a grain size of about 4.9 μm and a refinement of 55.8%. After aging treatment, a minor change in grain size was observed for V-free and V-containing steels with a grain size of approximately 12 μm and 5.3 μm, respectively. This reveals that the aging treatment at 600 °C has little effect on the grain size.

Fig. 5a and b shows TEM images of the V-free and V-added steels after annealing, confirming the results observed in Figs. 3 and 4, where the grain size of the V-added steel is significantly refined. It is noteworthy that the appearance of κ-carbide is not observed in both sheets of steel, as is shown in the selected area electron diffraction (SAED) pattern in Fig. 5a and b, which is consistent with the results calculated from the phase diagram in Fig. 1, which demonstrate a dissolution temperature of 770 °C for κ-carbide. However, a nanoscale V precipitated phase with a size of about 85 nm was found within the austenite matrix in the VA90 specimen. This V-rich phase was identified as a VC by SAED and energy-dispersive X-ray spectroscopy (EDS) mapping analysis (Fig. 5c and d).

After aging, no significant changes in austenite grain size were observed for the V-added and V-free steels. However, the presence of ordered phases was observed in addition to the austenite matrix (Fig. 6) in the AG60 steel. Corresponding SAED (Fig. 6b) patterns and high-resolution TEM (HRTEM) (Fig. 6c) observations confirmed the presence of such ordered

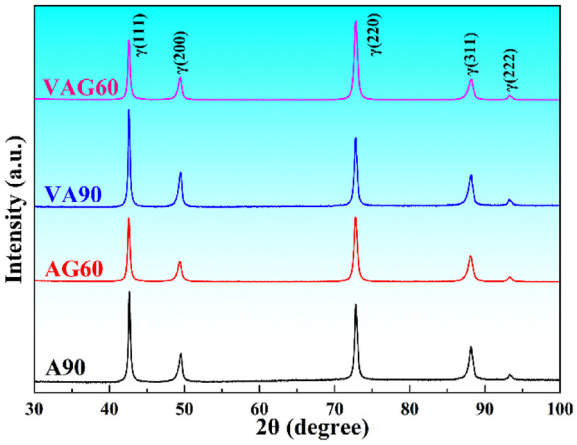

Fig. 2 – XRD patterns of the V-free and V-added steel after annealing and aging.

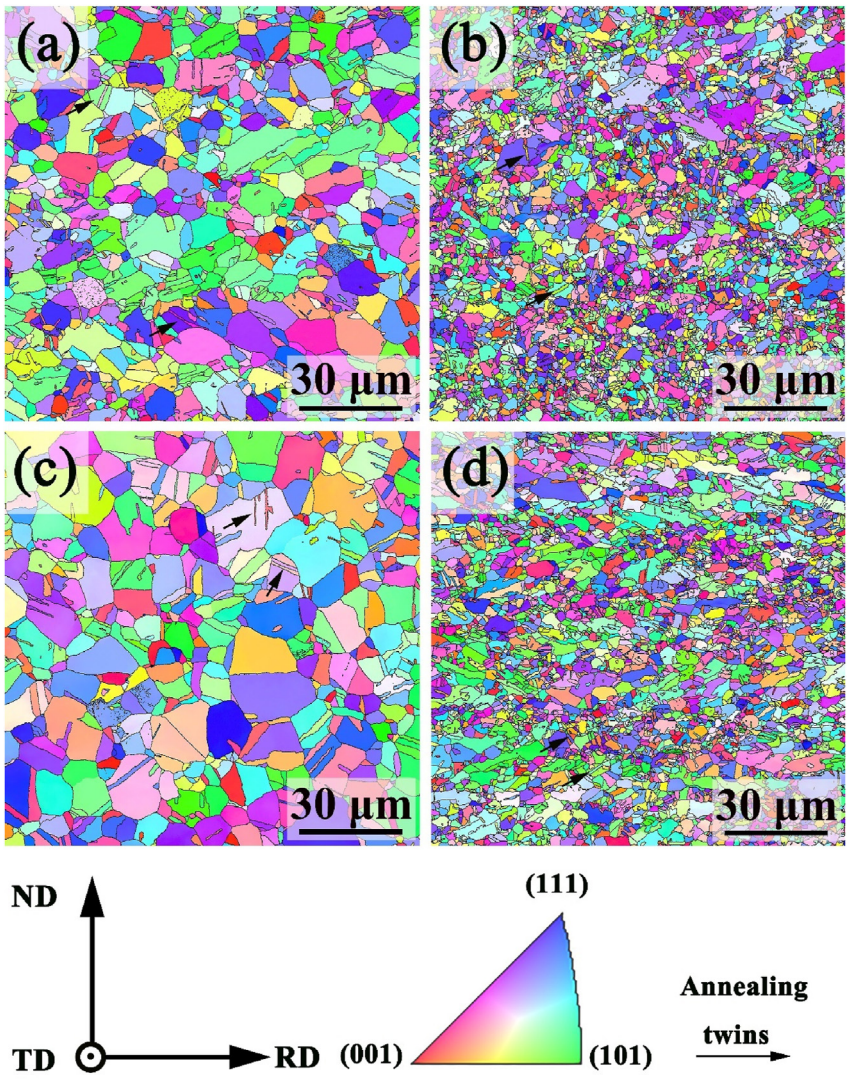

Fig. 3 – EBSD rolling direction (RD) inverse pole figure (IPF) maps of (a) and (b) the annealed specimens, (c) and (d) the aged specimens; (a) and (c) for the V-free steel, (b) and (d) for the V-added steel.

nanoscale grains within the austenite matrix. These SAED and the Fast Fourier transform (FFT) patterns of the ordered phase within the austenite matrix are consistent with those of κ-carbide. This nanoscale κ-carbide is uniformly distributed within the austenite grains with a size of about 4 nm. It is difficult to calculate the volume fraction due to its fine size. Compared to those in VA90 steel, the size of the VC particles in the VAG60 steel increased slightly after aging at 600 °C (Fig. 7a). It is noteworthy that after aging, VAG60 steel exhibits κ-carbide in addition to VC particles. However, the volume fraction of κ-carbide is substantially lower compared to the AG60 steel, which is confirmed by the weaker brightness of the spots in the SAED pattern (indicated by the red arrow) of Fig. 7b.

3.2. *Mechanical properties and deformation microstructure*

Fig. 8 shows the tensile stress–strain curves for the A90, VA90, AG60, and VAG60 specimens and strain hardening rate as a function of true strain. The engineering stress–strain curves until fracture 8, as shown in Fig. 8a, respectively. All specimens exhibit an excellent combination of strength and ductility, with ultimate tensile strengths exceeding 1000 MPa, while total elongation (TE) exceeds 40% (Fig. 8b). As shown in Table 1, the YS and ultimate tensile strength (UTS) of the annealed A90 specimens were 623 MPa and 1086 MPa, respectively, with a TE of 52%. When 0.5 wt% V element was added, the YS of the VA90 specimens increased to 827 MPa, an increase of about 25%, while the TE decreased slightly to 45%. After aging at 600 °C, the YS of both V-free and V-added steels increased substantially to 896 MPa and 1009 MPa, respectively, while exhibiting excellent TE of 46% and 41%, respectively. Both nanoscale VC and κ-carbide can effectively increase the strength of the material with less effect on ductility. It can be found that substantially increased the YS of the material with the combined effect of the two-type carbides precipitate comparing the YS of A90 and VA60. In this study, the test steel exhibits an excellent combination of strength and ductility compared to other lightweight austenitic steels [9,14,26,33–37], as shown in Fig. 8d.

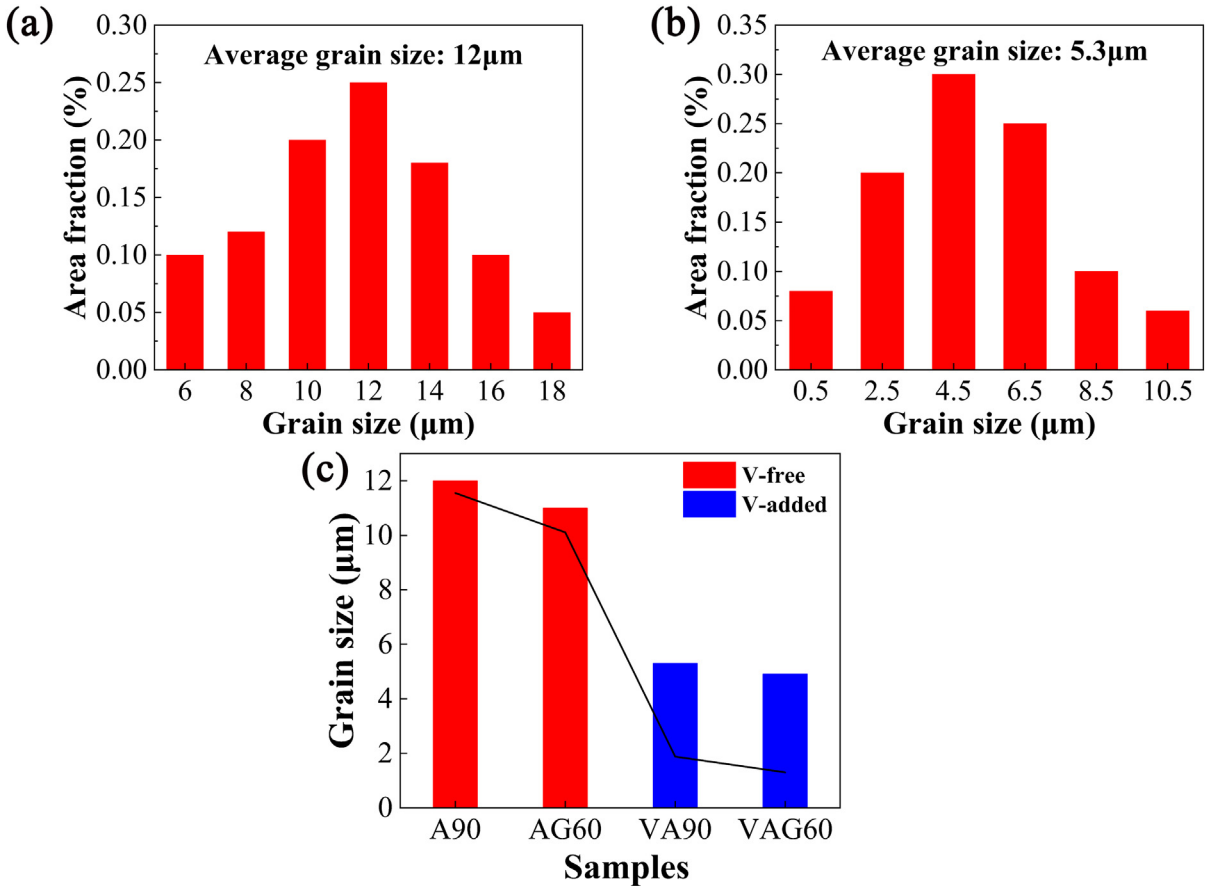

Fig. 4 – The grain size of the test steel was calculated by EBSD. (a) A90 steel; (b) VA90 steel; (c) the trend of grain size in different states.

The working hardening behavior is shown in Fig. 8d, which reported the strain hardening rate as a function of the true strain. Generally, the work hardening rate of the annealed A90 and VA90 specimens increases rapidly to a maximum value and then decreases with increasing strain until necking. The work hardening rate of AG60 and VAG60 specimens after aging was lower than that of annealed specimens. Aging reduces the work hardening rate of the alloy, which is common in aged Fe–Mn–Al–C lightweight steels [24,26]. The trend of the work hardening rate of VAG60 specimens is similar to that of annealed specimens. It is noteworthy that the work hardening rate of AG60 specimens gradually decreases with increasing strain until necking.

The main deformation mechanism of the material is planar dislocation slip in the high Mn lightweight steel, where dislocations usually slip in the plane, and the pronounced planar slip behavior leads to the formation of crystal alignment slip bands [38]. The microstructure after deformation of the aged steels was observed by TEM, and the representative results are shown in Figs. 9 and 10. Fig. 9a shows the microstructure of AG60 specimens at different strains; when the true strain $\varepsilon = 5\%$ (Fig. 9a), the development of planar slip bands appears in the specimen (indicated by yellow dashed lines), with a slip band spacing of 1.2 μm. When the true stress $\varepsilon = 10\%$, as in Fig. 9b, another set of slip systems is activated, and crossed slip bands appear while the slip band spacing decreases to 320 nm. Fig. 10a and b demonstrate the microstructure in the VAG60 specimen at true strain $\varepsilon = 5\%$, with a large number of dislocation entanglements and high-density dislocation walls (HDDWs) observed. In addition, dislocation tangles were observed in the vicinity of the VC particles. When the true stress $\varepsilon = 10\%$, As shown in Fig. 10c, the planar slip bands were observed in the VAG60 specimen, which was typical of planar slip and the SAED pattern confirmed the presence of κ-carbide in the VAG60 specimen. The dislocation cell formation is observed in addition to HDDWs indicated by red arrows in Fig. 10d. Fig. 10e shows a high magnification plot at the red dashed box in Fig. 10d with dense dislocation entanglement between the HDDWs. VC has a strong pegging effect on dislocations, and dense dislocation entanglement is observed near VC particles (Fig. 10f).

3.3. *Fracture analysis*

Fig. 11 represents the fracture morphology of the studied lightweight steel after uniaxial tensile testing at room

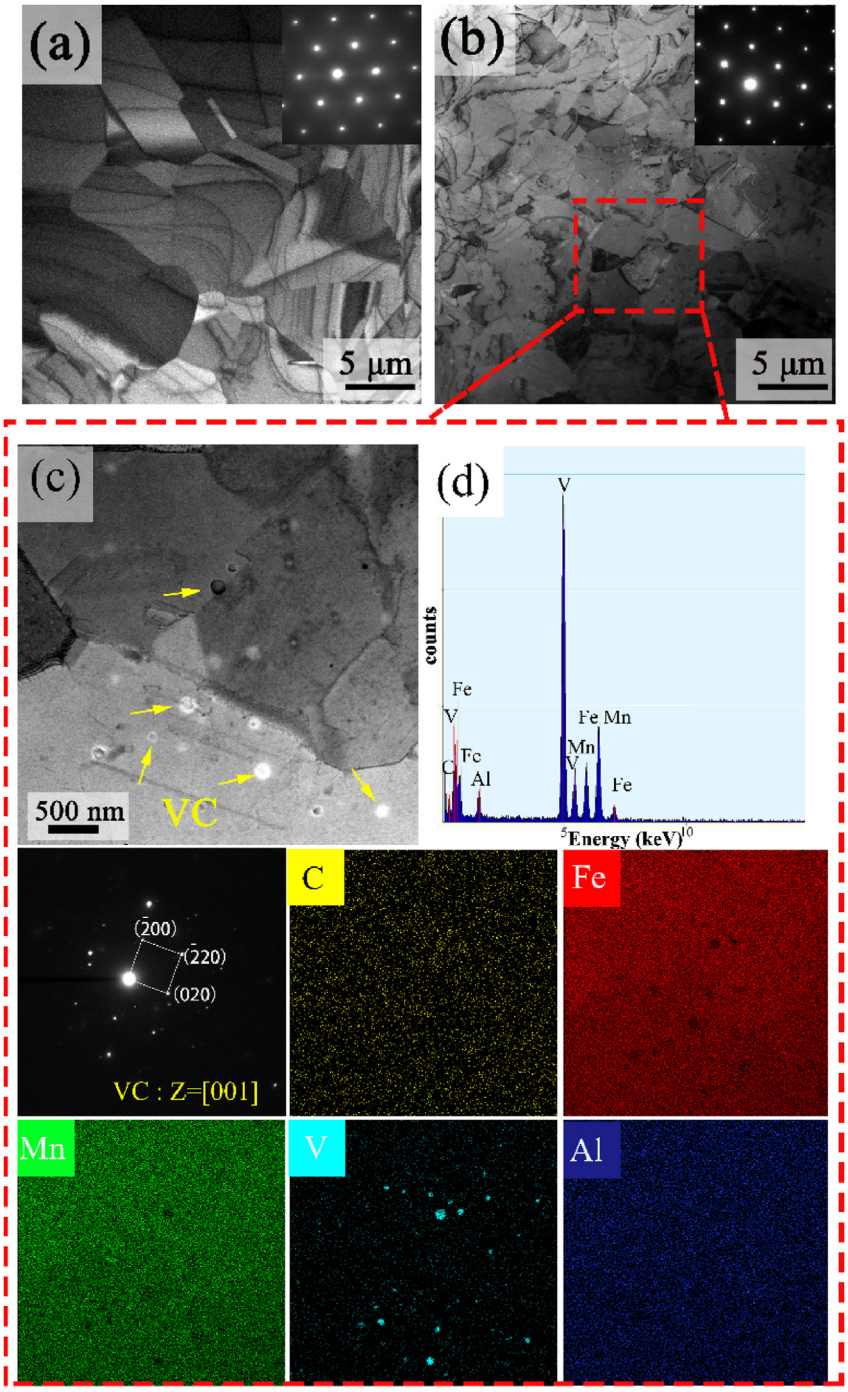

Fig. 5 – TEM bright-field image and corresponding SAED patterns of the specimen (a) A90 and VA90 (b); (c) Magnified micrograph of the red dotted box in (b); (d) EDS analysis and SAED pattern revealing the presence of VC particles in the austenite matrix.

temperature. A typical ductile fracture of the ductile-like morphology was observed in the A90, VA90, AG60, and VAG60 specimens (Fig. 11). The morphology of the fracture is shown in the corresponding insets. The fracture morphology of these specimens was taken in the fibrous zone. The presence of deep dimples and initial microvoids suggests the initiation of material failure. As shown in Fig. 11a, the fracture morphology of specimen A90 has a uniform distribution of deep dimples, which indicates a uniform distribution of initial microvoids. As a result, the A90 specimen exhibited excellent ductility (up to 52%). According to the theory proposed by Thomson et al. [39], the nucleation, growth, and eventual merging of microvoids dominate the micro-crack formation in the material. As shown in Fig. 11b, smaller and shallow dimples are observed in the fracture morphology of VA90 specimens containing V. After aging, the fracture

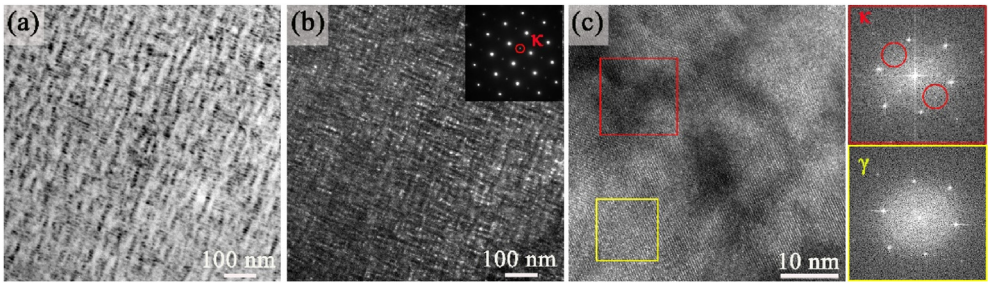

Fig. 6 – TEM and HRTEM micrographs of the AG60 specimen: (a) bright-field and (b) dark-field images of κ-carbide nanoparticles within the austenite matrix; (c) zone axis of HRTEM images of austenite, and corresponding FFT patterns revealing the presence of κ-carbide.

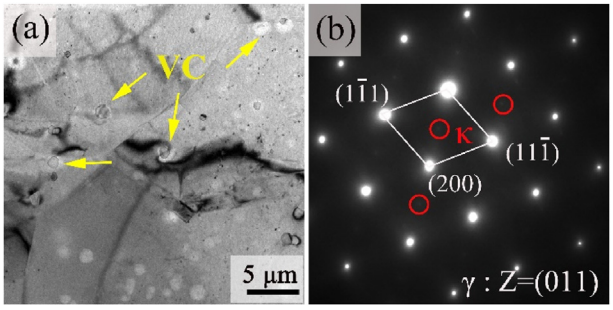

Fig. 7 – TEM image of the VAG60 specimen. (a) BF TEM image showing VC particles. (b) SAED image revealing the presence of few κ-carbide indicated by the red circle.

morphology of the AG60 and VAG60 specimens did not change significantly compared with the annealed condition. Still, the number of microvoids was greater, and the dimples were more shallow. Therefore, it can be concluded that the dimple type's ductile fracture dominates the material's fracture behavior, which is consistent with the excellent ductility of the material (TE > 40% for all specimens). Microalloying of V elements and aging treatment did not change the fracture behavior of the material, and the fracture form is still a ductile fracture.

4. Discuss

4.1. *Precipitation behavior of VC*

In this study, a two-step heat treatment is carried out to promote the precipitation of different nanoparticles and to understand their interactions. A schematic diagram of the formation of the two nano-sized precipitates is shown in Fig. 12a. After annealing, only the austenite phase is observed for the V-free steel. By contrast, nanoscale VC particles are observed for the V-added steel and austenite (Fig. 5c). In general, V microalloying was used to strengthen ferritic and martensitic steels with a BCC structure, where the precipitation of nano-sized VC particles and grain refinement effectively increase the YS of the steel [40]. Given the high solid solubility of V in austenitic steels, the volume fraction of VC particles is constrained. However, the volume fraction of VC particles here is more considerable (Fig. 5). After aging, the formation of nanoscale κ-carbides in V-free steels was formed observed in maintaining a coherent relationship with austenite (Fig. 6). The formation of such κ-carbides is reported by spinodal decomposition after quenching or aging [19]. The fluctuation and segregation of Al and C elements significantly affect κ-carbides, and the minimum solute content required for κ-carbides during water quenching is reported in the literature (Al > 7% and C > 0.8%) [14]. The presence of κ-carbide was also observed in the VAG60 specimens after aging. Still, its volume is few (Fig. 7b). The volume of κ-carbide decreased substantially in the VAG60 specimens and was closely related to the precipitation of particles of VC. It is well known that adding V to steel is highly susceptible to carbide formation with C [32]. The formation energies of two precipitation phases, VC and κ-carbide, were analyzed by first-principles calculations as −0.411 and −0.161 eV. The formation energy of the VC precipitation phase is much lower than that of κ-carbide, which means that the VC precipitation phase is more stable in austenite [37]. In addition, according to the calculations in Fig. 1b, VC does not dissolve until 1080 °C, which means that it is very stable during aging at 600 °C. Therefore, it is shown that the C element is enriched near the VC particles, resulting in an austenite matrix poor in C elements, suppressing the precipitation of κ-carbide (Fig. 5). This finding is confirmed by the Vickers hardness result (Fig. 12b). Under the annealed condition, the precipitation of VC particles results in a higher hardness of V-added steels than V-free steels. However, the hardness of the V-free steel is higher than that of the V-added steel under aged conditions, indicating that the volume fraction of κ-carbide is greater in the V-free steel than in the V-added steel. Furthermore, this result confirms that VC suppresses the precipitation of κ-carbide.

4.2. *Effect of V addition on the microstructure*

The V microalloying is known to be effective in refining the grain size of steel. The grain sizes of the A90 and VA90 specimens were 9.9 μm and 4.9 μm, respectively. It can be seen that the grain size of the annealed V-added steel is significantly

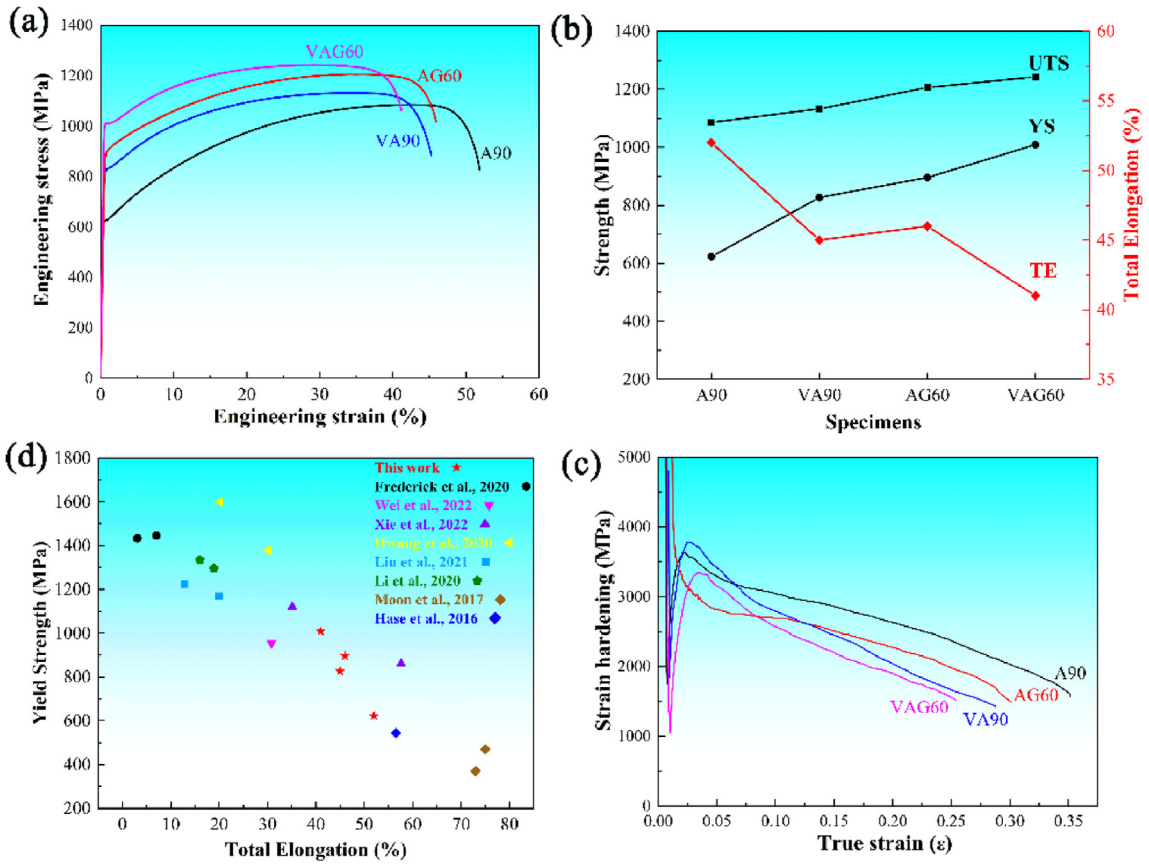

Fig. 8 – (a) Engineering stress–strain curves. (b) Changes in strength and elongation of annealed and aged steel. (c) Tensile properties of the present steel compared to other lightweight austenite steel. (d) Strain hardening rate as a function of the true strain of the annealed and aged steel.

Table 1 – Tensile properties of V-free and V-added steels after annealing and aging.

Specimen		Yield Strength (MPa)	Tensile Strength (MPa)	Uniform Elongation (%)	Total Elongation (%)
As-annealed	A90	623	1086	42	52
	VA90	827	1133	34	45
As-aged	AG60	896	1206	35	46
	VAG60	1009	1243	29	41

finer (Fig. 3a) compared to the V-free steel (Fig. 3b). This grain refinement mechanism is strongly related to the VC particles precipitating during annealing. Based on other previous studies, V alloying may have retarded the recrystallization of the experimental steel slightly, resulting in grain size refinement [32]. However, this phenomenon was not observed in the present study. The Grain Orientation Spread (Fig. 13) maps before tensile deformation were used to describe the degree of recrystallization of the test steel. The results showed that V microalloying has a small effect on the degree of recrystallization in test steel, as V-added and V-free steels achieve almost full recrystallization. The possible effect of the addition of V on the recrystallization behavior of the cold-rolled steel has not been established, and it will require further

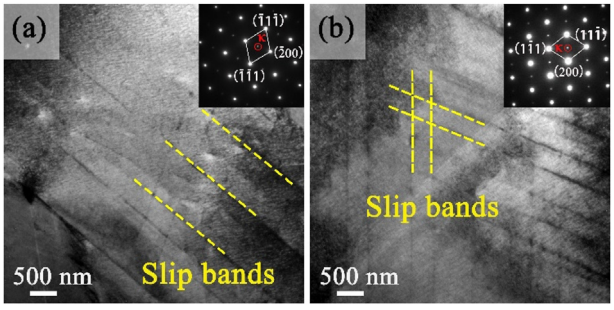

Fig. 9 – Dislocation structures in the AG60 sample at a true strain of (a) 5% and (b) 10%. (Dashed and dotted lines indicate plane slip bands in the austenite).

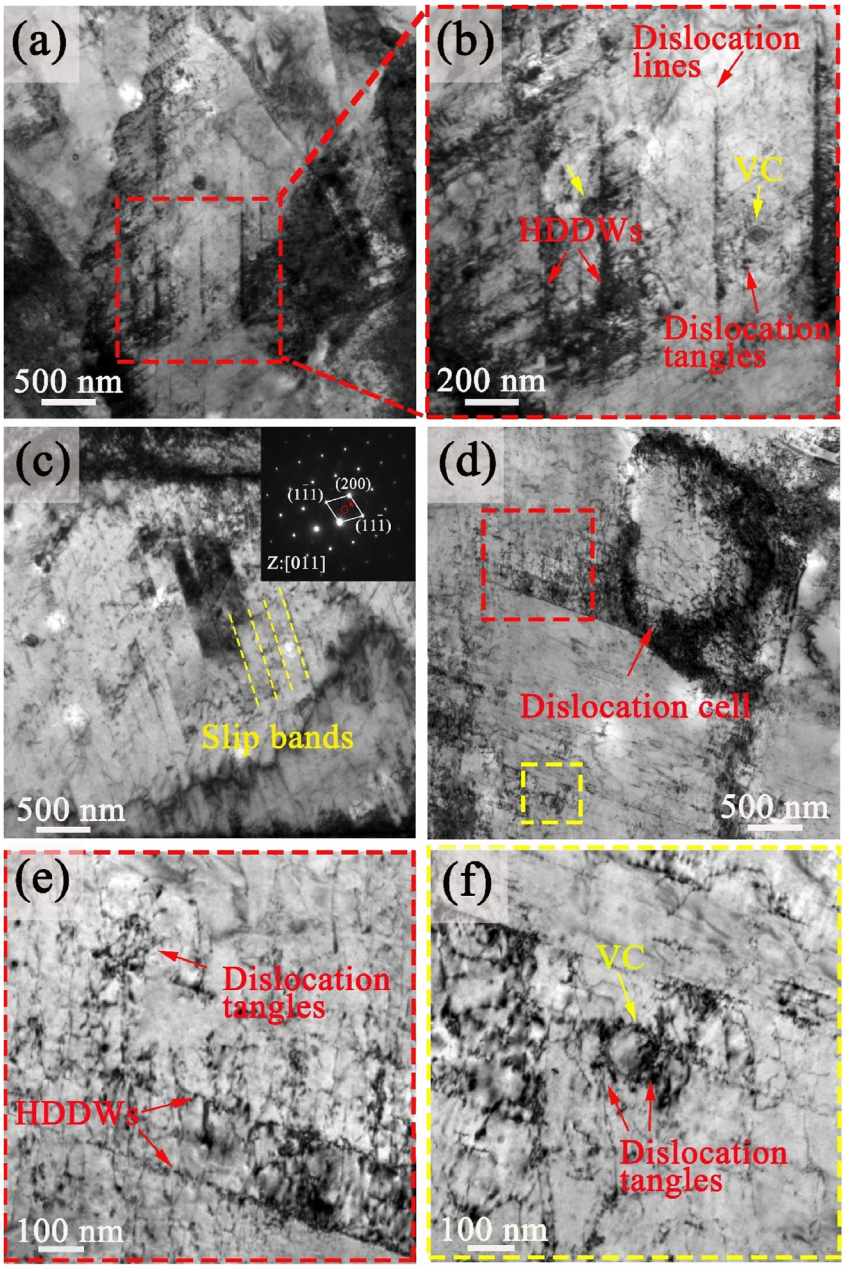

Fig. 10 – Dislocation structures in the VAG60 sample at a true strain of (a and b) 5% and (c, d, e, f) 10%. (b) magnified micrograph of dislocation in (a) shows the HDDWs and dislocation tangles. The slip bands and dislocation are observed in (c) and (d), respectively. (e), and (f) the magnified micrograph of the red and yellow dotted box, respectively, in (d) showing dislocation tangles near the slip band and VC particles.

work. More details about recrystallization are illustrated using kernel average misorientation (KAM) maps (Fig. 14) and corresponding statistics. The results showed that the average value of KAM was higher for V-added steels than for V-free steels, particularly at the grain boundaries. This difference is attributed to the presence of a considerable amount of VC precipitates, which is due to the pinning effect of VC on the austenite grain boundaries, which hinders the growth of the austenite grains. Therefore, the grain size of V-added steels was smaller than that of V-free steels. After aging, no significant changes in grain size were observed in AG60 and VAG60 specimens compared with their respective annealed specimens. This shows that the precipitation of κ-carbide has almost no effect on the austenite grain size.

4.3. *Effect of V addition on the mechanical properties*

The YS of test steel is usually subject to the combined effect of multiple strengthening mechanisms, expressed by the following equation [41]:

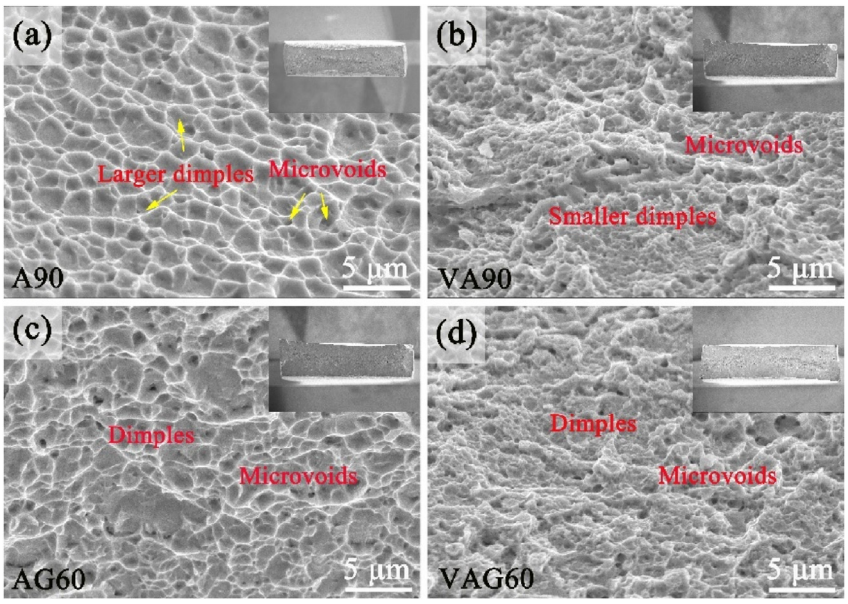

Fig. 11 – SEM fracture morphologies of the A90, VA90, AG60 and VAG60 samples. The macroscopic features of the fracture surfaces of the present steel are inserted in the upper right corner.

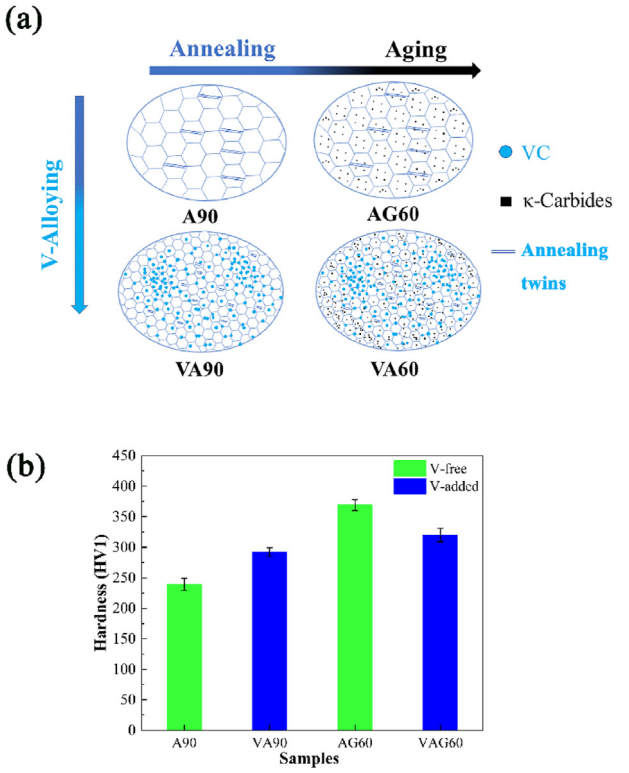

Fig. 12 – (a) A schematic diagram of the formation of VC and κ-carbide. (b) The Vickers hardness of annealed and aged steel.

$$\sigma_{YS} = \sigma_0 + \sigma_g + \sigma_p + \sigma_d \quad (1)$$

where σ_{YS} refers to the YS, σ_0 includes the lattice friction stress and solid solution strengthening of alloying elements, σ_g refers to the grain boundary strengthening, σ_p refers to precipitation strengthening, and σ_d refers to the dislocation strengthening.

σ_0 Is expressed by the following empirical formula [42]:

$$\sigma_0 = 279\ wt.\%\ C - 1.5\ wt.\%\ Mn + 20.5\ wt.\%\ Al \quad (2)$$

where wt.% í (í: C, Mn, Al, and V) is the weight percentages dissolved in austenite, respectively, which are determined by TEM-EDS (for Al, Mn, and Fe) and the lever rule (for C). The calculation of solid solution hardening also considers the effect of VC precipitation on solute C, which is almost negligible. σ_g is calculated using the Hall-Petch relation as follows [42]:

$$\sigma_g = k_{HP} d^{-1/2} \quad (3)$$

where d is the average size of austenite grain (μm), and k_{HP} is the Hall-Petch coefficient (461 MPa $\mu m^{1/2}$ [42]). The precipitation strengthening mainly results from nano-sized VC particles interacting with dislocation by the Orowan bypassing mechanism, and κ-carbides interact with dislocation by the shearing mechanism. It should be noted that nanoscale κ-carbides particles to the strength of aged specimens are not considered since it was not possible to measure their fractions due to their very fine sizes reliably (<5 nm) detectable by TEM. Here, the precipitation strengthening is mainly calculated from the contribution of VC particles, which can be estimated based on the Orowan strengthening mechanism. The strengthening contribution of the VC particles by the Orowan mechanism can be expressed as follows [33]:

$$\sigma_{p-VC} = M \frac{0.4Gb}{\pi\sqrt{1-\upsilon}} \frac{\ln(2r^*/b)}{2r^*\left(\sqrt{\frac{\pi}{4f}} - 1\right)} \quad (4)$$

where M is the Taylor factor (3.06) [43]; G and b are the shear modulus and magnitude of the Burgers vector of austenite (70 GPa and 0.26 nm) [43], respectively; υ is the Poisson's ratio

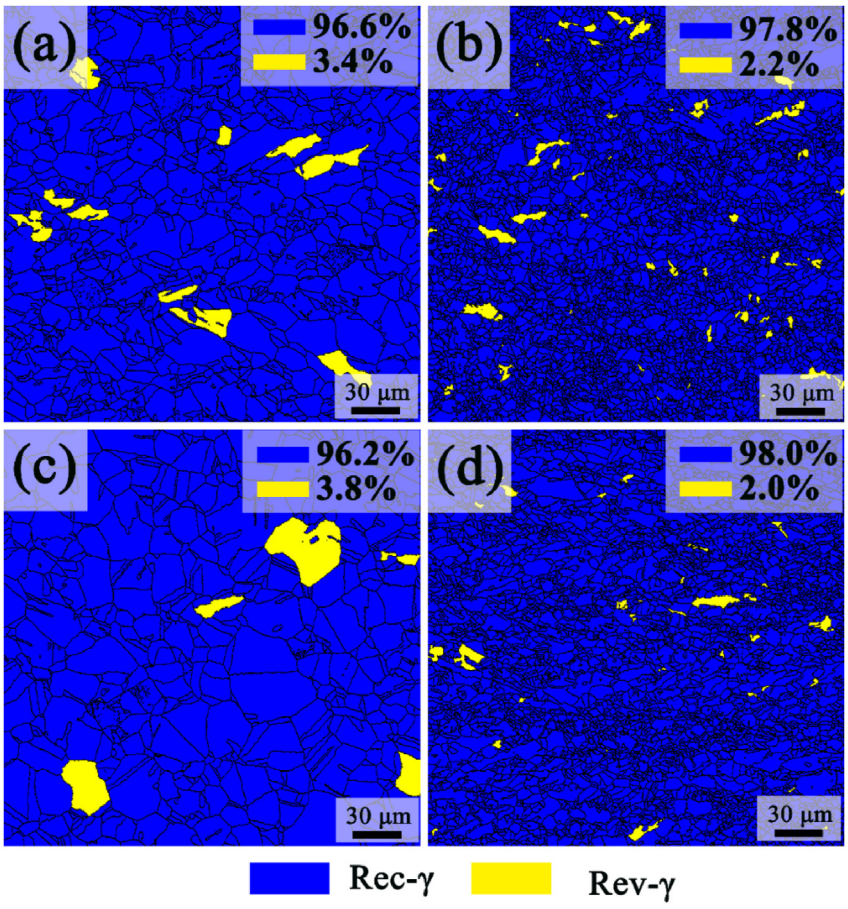

Fig. 13 – Grain Orientation Spread maps and statistical results: (a) A90; (b) VA90; (c) AG60; (d) VAG60. (Rec-γ: Recrystallized austenite, Rev-γ: Non-Recrystallized austenite).

(0.33) [33]; $r^* = (2/3)^{0.5}d/2$, and d and f are the average size and volume of the VC precipitates, respectively. The Bailey–Hirsch relationship was used to estimate dislocation strengthening [43]:

$$\sigma_d = M\alpha Gb\rho^{0.5} \quad (5)$$

where α is a constant (0.2) [43] and ρ is the dislocation density. In the present study, the dislocation strengthening results from the geometrically necessary dislocations (GNDs) since the densities of retained statistically stored dislocations after annealing were very small and negligible [43,44]. The following expression can calculate the density of GNDs [45]:

$$\rho = 2\theta/\mu b \quad (6)$$

where θ is the misorientation angle and μ is the unit length ($\mu = 10^{-5}$ m) [44]. The misorientation angle can be calculated by EBSD analysis, which gives the dislocation density of A90, VA90, AG60, and VAG60 specimens as 9.9×10^{13} m^{-2}, 10.3×10^{13} m^{-2}, 9.1×10^{13} m^{-2} and 9.5×10^{13} m^{-2}, respectively.

The contributions of individual strengthening factors to the YS of steels with and without V are shown in Table 2, and the corresponding column graphs are given in Fig. 15. The comparative agreement between the calculated and experimentally obtained YS of annealed steels illustrates the reasonableness of this calculation method. The annealed V-added steel achieves a higher contribution of grain boundary strengthening and VC particle precipitation strengthening than the annealed V-free steel, resulting in a YS increase of ~200 MPa. After aging, the YS of both the V-free and V-added steel are substantially increased, mainly due to the precipitation strengthening of κ-carbide. It is worth noting that the volume fraction of κ-carbide cannot be accurately counted due to its small size, resulting in the precipitation strengthening the contribution of κ-carbide cannot be obtained directly by calculation. As shown in Table 2, there is a significant difference between the calculated and experimental values of the YS of the aged steel after aging. This difference mainly originates from the precipitation strengthening of the κ-carbide. As shown in Fig. 15 and Table 2, the precipitation strengthening of κ-carbide is lower in VAG60 steel than in AG steel (218 MPa vs. 276 MPa), which is due to the inhibition of κ-carbide precipitation by the precipitation of VC particles, reducing the volume fraction of κ-carbide (Fig. 7). However, the grain boundary strengthening (~208 MPa) and precipitation strengthening of VC particles (~115 MPa), in addition to precipitation strengthening of κ-carbide, contributed significantly to the yield strength of the VAG60 specimen, resulting in a higher yield strength of the VAG60 specimen. Overall, the effective combination of fine-grained strengthening, nano-sized VC particles, and κ-carbide precipitation strengthening

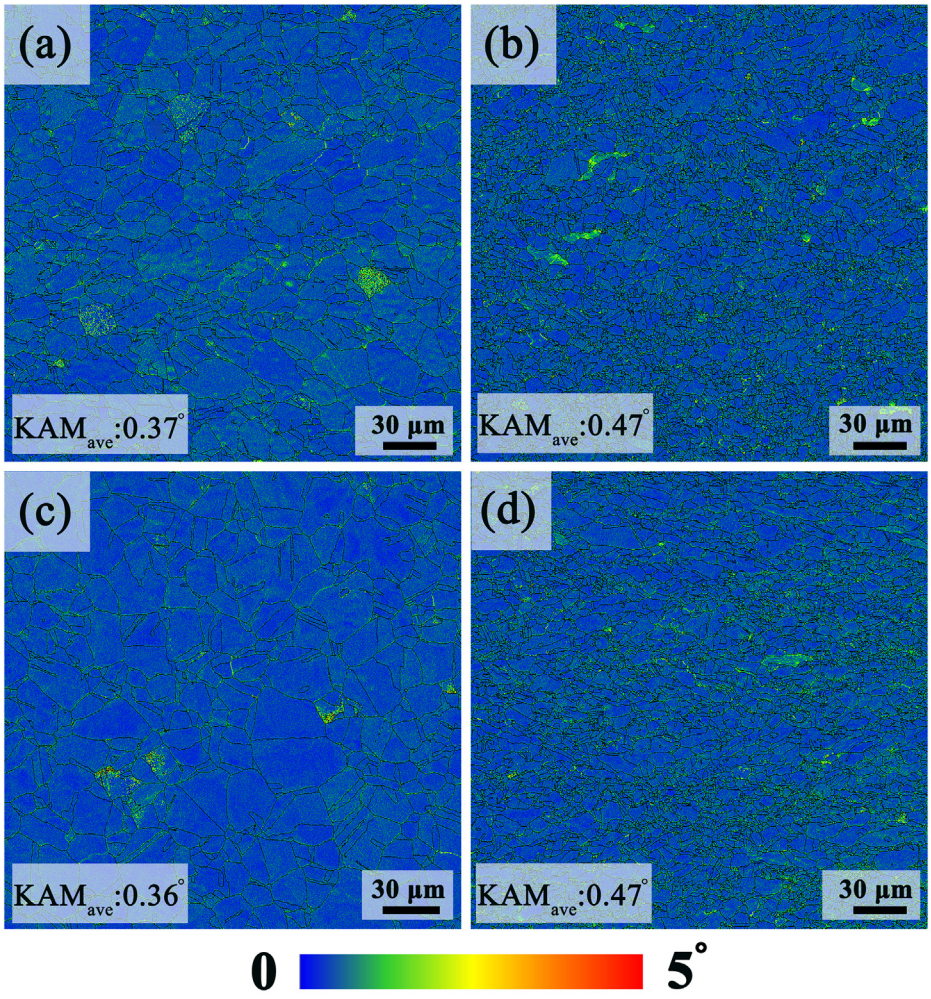

Fig. 14 – Kernel average misorientation maps and statistical results: (a) A90; (b) VA90; (c) AG60; (d) VAG60.

in V-added steels causes a considerable increase in the YS of lightweight steels.

The volume fraction of VC precipitates in V-added steel does not change significantly after aging at 600 °C compared to the annealed state, and the precipitation of VC particles is limited at low-temperature aging. κ-Carbide can precipitate in high-density at low-temperature aging, but the character of being easily cut by dislocations lead to low strain hardening ability. Therefore, the coexistence of the dual-nanoprecipitation after aging can compensate for the deficiencies of each in precipitation strengthening. A dual-precipitation structure consisting of VC and κ-carbide can effectively enhance the material's mechanical properties.

4.4. *Effect of V addition on the strain hardening*

As shown in Fig. 8d, adding V significantly affects the strain hardening rate of both annealed and aged lightweight steels. The hardening mechanism of nano-sized κ-carbide and VC particles on lightweight steels during deformation needs to be clarified. In the annealed condition, the work hardening rate of V-added steels was higher than that of V-free steels under tensile strains below 6% (Fig. 8d), caused by the strongly hindering effect of nano-sized VC particles on the moving dislocations during the tensile deformation. As the tensile strain increased (>6%), the work hardening rate of V-added steels was lower than that of V-free steels, which was related to the

Table 2 – The calculation results of the contribution of various strengthening mechanisms.

Specimen	σ_0	σ_g	$\sigma_{p\text{-}vc}$	σ_d	$\sigma_{YS\text{-}1}$ (*estimated*)	$\sigma_{YS\text{-}2}$ (*experimental*)	$\sigma_{p\text{-}\kappa}$ ($\sigma_{YS\text{-}2}$ – $\sigma_{YS\text{-}1}$)
A90	378	133	–	111	622	623	–
VA90	374	200	115	113	802	827	–
AG60	367	147	–	106	620	896	276
VAG60	359	208	115	109	791	1009	218

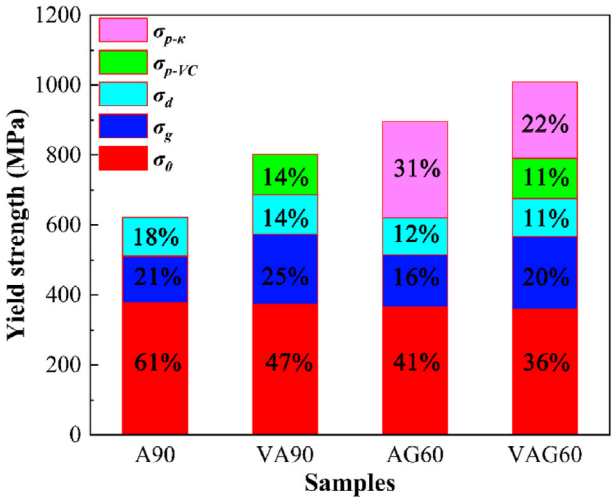

Fig. 15 – Contribution of individual strengthening factors to yield strength in the A90, VA90, AG60, and VAG60 samples.

strain localization caused by VC particles [36,37]. After aging treatment, κ-carbides precipitated in both V-added and V-free steels. The work-hardening rate of VAG60 specimens was affected by both VC and κ-carbides. κ-Carbide precipitation has been intensively investigated in aged lightweight steels as an important strengthening method [4,24]. κ-Carbide can effectively increase the strength of lightweight steel; however, it reduces the strain hardening rate (Fig. 8d), which has also been confirmed in other studies [24,25]. This is because the κ-carbide can be cut through by moving dislocations, causing a so-called glide plane softening effect [26]. As the motion of the first dislocation on the slip surface disrupts the locally ordered structure, it leads to a decrease in the slip resistance of subsequent dislocations on the slip surface and a strain softening on the glide plane [24,46]. Therefore, the κ-carbide in the AG60 specimen was continuously cut by the dislocations, which reduced the hindering effect on the dislocation slip, resulting in a continuous decrease in the strain hardening rate with increasing strain. However, the precipitation of hard and non-shearable VC particles in the VAG60 specimens effectively increased the strain hardening rate of the lightweight steel in the early stages of deformation compared to the AG60 specimens containing only κ-carbides (Fig. 8d). This is because the VC particles lead to the plugging of dislocations in the vicinity of the particles, which not only significantly increases the dislocation density, but also changes the local distribution of dislocations (Fig. 10). Although the volume fraction of nano-scale VC particles is small, it can effectively improve the lightweight steel's YS and strain hardening rate. VC particles with the Orowan bypassing mechanism can effectively compensate for the lower work hardening rate due to shearable κ-carbide in the early stages of deformation. Thus, the effective combination of both VC and κ-carbide particle precipitation can produce greater strengthening effects.

Fig. 9a and b shows the dislocation structures of the AG60 specimens at strains $\varepsilon = 5\%$ and $\varepsilon = 10\%$, respectively. The corresponding insets are SAED plots revealing the presence of κ-carbide. With increasing strain, the deformation structure is characterized by continuous refinement of the spacing between the slip bands and an increase of the intersecting slip bands. This is strongly related to the feature that the κ-carbide can be cut through by dislocations, as confirmed in other aged steels [4]. No appearance of deformation twins was observed, at which point the strain hardening mechanism of the aged lightweight steel was the refinement of the slip bands. The increasing number of such slip bands and their decreasing spacing result in a strong increase in the stored dislocation density. The dislocation cutting frequency leads to an increase in passing stress, which contributes to strain hardening [4,38]. Fig. 10 illustrates the dislocation structure of VAG60 specimens at different strains. VC and a small amount of κ-carbide can be observed in the VAG60 specimens. Fig. 10a and b shows the dislocation structure at strain $\varepsilon = 5\%$, where HDDWs and dislocation entanglement near VC particles are observed. No significant slip band is observed, and the main reason for the reduced slip band activity is the substantially lower volume fraction of κ-carbide. As shown in Fig. 10c, the planar slip bands were observed in the VAG60 specimen, which was typical of planar slip. This was attributed to the precipitation of κ-carbide in the austenite matrix, which was consistent with the experimental results observed in their study [4,25]. It has been reported that the appearance of shear-orderable precipitates in face-centered cubic solid solution alloys is responsible for the planarity of dislocation slips, which caused by the phenomenon of softening of the slip plane [25]. The addition of V reduces the volume fraction of ordered κ-carbide in VAG60 specimens, decreasing the activity of planar slip and has an effect on the dislocation slip mechanism of the specimens. Therefore, dislocation cell (Fig. 10d) was observed when the strain was increased to $\varepsilon = 10\%$, which was a typical kind of wavy-slip type dislocation structure. At the same time, many dislocations were plugged near the VC particles, leading to dislocation entanglement (Fig. 10e). Thus, it is concluded that the precipitation of VC accelerates the rate of dislocation accumulation during plastic deformation. The strain hardening rate is higher for aging steels containing nano-sized VC particles in early states of deformation than lighter steels without VC particles. VC particles compensate for the abrupt drop in the strain hardening rate at the beginning of deformation due to κ-carbide that can be cut through by dislocations and improve the hardening ability of lightweight steel.

The combined effect of nano-sized VC and κ-carbide significantly strengthens the lightweight steel while ensuring excellent ductility.

5. Conclusions

(1) The grain size of austenite was significantly refined from 9.9 to 4.9 μm with the addition of V in the annealed state, which is primarily attributed to the pegging of austenite grain boundaries with VC particles. After aging, no significant changes in grain size were observed for V-free and V-added steels.

(2) Nano-sized VC and κ-carbide particles precipitate in the austenite matrix after annealing and aging. Simultaneously, the precipitation of κ-carbide was

suppressed due to the C-poor solute in the austenite matrix caused by the precipitation of VC particles.

(3) A two-step heat treatment, including annealing and aging, is taken to promote the precipitation of VC and κ-carbide particles, thus substantially improving the strength of the material. The yield and UTS of aged V-added specimens reached 1009 MPa and 1243 MPa, respectively, and the TE reached 41%. The aged V-added steels exhibit an excellent combination of tensile strength and ductility, mainly resulting from grain boundary strengthening and dual-nanoprecipitation strengthening.

(4) The strain hardening rate of the V-free steel decreases as κ-carbide precipitates after aging. With the addition of V, this deficiency is compensated. The precipitation of non-shearable VC particles in the austenite grains effectively pins dislocations during deformation and improves the strain hardening rate of the aged steel in the initial stages of deformation. The synergistic effect of VC and κ-carbide ensures a high hardening capacity, consequently increasing the lightweight steel's tensile strength.

Data availability

The raw and processed data required to reproduce these findings cannot be shared at this time as the data also forms part of an ongoing study.

Declaration of competing interest

We declare that we have no known competing financial interests or personal relationships that could have appeared to influence the work reported in this paper.

Acknowledgments

This work was supported by the National Natural Science Foundation of China (Grant No. 52127808, 52125405 and U22A20108), the Open of Key Laboratory of New Processing Technology for Nonferrous Metal & Materials, Ministry of Education (No. 20KF-10) and the Hebei Provincial Department of Education Funding Project for Cultivating Innovative Ability of Graduate Students (No. CXZZBS2023047).

REFERENCES

[1] Choi K, Seo CH, Lee H, Kim SK, Kwak JH, et al. Effect of aging on the microstructure and deformation behavior of austenite base lightweight Fe–28Mn–9Al–0.8C steel. Scripta Mater 2010;63(10).

[2] Kim H, Suh DW, Kim NJ. Fe–Al–Mn–C lightweight structural alloys a review on the microstructures and mechanical. Sci Technol Adv Mater 2013;14.

[3] Chen S, Rana R, Haldar A, Ray RK. Current state of Fe-Mn-Al-C low density steels. Prog Mater Sci 2017;89.

[4] Yao MJ, Welsch E, Ponge D, S.M.H, et al. Strengthening and strain hardening mechanisms in a precipitation hardened high-Mn lightweight steel. Acta Mater 2017;140.

[5] Zambrano OA. A general perspective of Fe–Mn–Al–C steels. J Mater Sci 2018;53(20).

[6] Li Z, Wang YC, Cheng XW, Li ZY, Gao C, et al. The effect of rolling and subsequent aging on microstructures and tensile properties of a Fe-Mn-Al-C austenitic steel. Mater Sci Eng, A 2021;822.

[7] Rena P, Chena XP, Cao ZX, Mei L, Lia WJ, et al. Synergistic strengthening effect induced ultrahigh yield strength in lightweight Fe-30Mn-11Al-1.2C steel. Mater Sci Eng, A 2019;752.

[8] Ji F, Song W, Ma Y, Li C, Bleck W, et al. Recrystallization behavior in a low-density high-Mn high-Al austenitic steel undergone thin strip casting process. Mater Sci Eng 2018;733.

[9] Moon J, Park SJ, Jang JH, Lee TH, Lee CH, et al. Atomistic investigations of κ-carbide precipitation in austenitic Fe-Mn-Al-C lightweight steels and the effect of Mo addition. Scripta Mater 2017;127.

[10] Ennis BL, Jimenez-Melero E, Mostert R, Santillan B, Lee PD. The role of aluminium in chemical and phase segregation in a TRIP-assisted dual phase steel. Acta Mater 2016;115.

[11] Sohn SS, Choi K, Kwak J-H, Kim NJ, Lee S. Novel ferrite–austenite duplex lightweight steel with 77% ductility by transformation induced plasticity and twinning induced plasticity mechanisms. Acta Mater 2014;78.

[12] Ha MC, Koo JM, Lee JK, Hwang SW, Park KT. Tensile deformation of a low density Fe–27Mn–12Al–0.8C duplex steel in association with ordered phases at ambient temperature. Mater Sci Eng, A 2013;586.

[13] Parka KT, Jin KG, Han SH, Hwang SW, Choid K, et al. Stacking fault energy and plastic deformation of fully austenitic high manganese steels: effect of Al addition. Mater Sci Eng, A 2010;527.

[14] Hwang JH, Trang TTT, Lee O, Park G, Zargaran A, et al. Improvement of strength-ductility balance of B2-strengthened lightweight steel. Acta Mater 2020;191.

[15] Raabe D, Springer H, Gutierrez-Urrutia I, Roters F, Bausch M, et al. Combinatorial synthesis, and microstructure– property relations for low-density Fe-Mn-Al-C austenitic steels. JOM 2014;66.

[16] Sato K, Tagawa K, Inoue Y. Modulated structure and magnetic properties of age hardenable Fe-Mn-Al-C alloys. Metall Trans 1990;21A:5–11.

[17] Cheng WC, Cheng CY, Hsu CW, Laughlin DE. Phase transformation of the L12 phase to kappa-carbide after spinodal decomposition and ordering in an Fe–C–Mn–Al austenitic steel. Mater Sci Eng, A 2015;642.

[18] Gutierrez-Urrutia I, Raabe D. Influence of Al content and precipitation state on the mechanical behavior of austenitic high-Mn low-density steels. Sci. Mater 2013;68.

[19] Sato K, Tagawa K, Inoue Y. Spinodal decomposition and mechanical properties of an austenitic Fe-30wt.%Mn-9wt.% Al-0.9wt.%C alloy. Mater Sci Eng, A 1989;111.

[20] Sato K, Tagawa K, Inoue Y. Age hardening of an Fe-30Mn-9Al-0.9C alloy by spinodal decomposition. Scripta Metall Mater 1988;22(6).

[21] Kimura Y, Handa K, Hayashi K, Mishima Y. Microstructure control and ductility improvement of the two-phase g-Fe/k-(Fe, Mn)3AlC alloys in the Fe–Mn–Al–C quaternary system. Intermetallics 2004;12.

[22] Chang KM, Chao CG, Liu TF. Excellent combination of strength and ductility in an Fe–9Al–28Mn–1.8C alloy. Sci. Mater 2010;63(2).

[23] Park KT. Tensile deformation of low-density Fe–Mn–Al–C austenitic steels at ambient temperature. Scripta Mater 2013;68.
[24] Kim SD, Park SJ, Jang Jh, Moon J, Ha HY, Lee CH, et al. Strain hardening recovery mediated by coherent precipitates in lightweight steel. Sci Rep 2011;11(14468).
[25] Wu ZQ, Ding H, An XH, Han D, Liao XZ. Influence of Al content on the strain-hardening behavior of aged low density Fe–Mn–Al–C steels with high Al content. Mater Sci Eng, A 2015;639.
[26] Haase C, Zehnder C, Ingendahl T, Bikar A, Tang F, et al. On the deformation behavior of κ-carbide-free and κ-carbide-containing high-Mn light-weight steel. Acta Mater 2017;122.
[27] Zhang J, Raabe D, Tasan CC. Designing duplex, ultrafine-grained Fe-Mn-Al-C steels by tuning phase transformation and recrystallization kinetics. Acta Mater 2017;141.
[28] Zhang G, Ma W, Tang Y, Wang F, Zhang X, et al. Investigation on the microstructural evolution and mechanical properties of partially recrystallized Fe-27Mn-10Al-1.4C steel. Mater Sci Eng, A 2022;833.
[29] Park G, Nam CH, Zargaran A, Kim NJ. Effect of B2 morphology on the mechanical properties of B2-strengthened lightweight steels. Scripta Mater 2019;165.
[30] Song H, Yoo J, Kim SH, Sohn SS, Koo M, et al. Novel ultra-high-strength Cu-containing medium-Mn duplex lightweight steels. Acta Mater 2017;135.
[31] Wang Z, Lu W, Zhao H, He J, Wang K, et al. Formation mechanism of κ-carbides and deformation behavior in Si-alloyed FeMnAlC lightweight steels. Acta Mater 2020;198.
[32] Gwon H, Kima JK, Shina S, Cho L, Coomana BCD. The effect of vanadium micro-alloying on the microstructure and the tensile behavior of TWIP steel. Mater Sci Eng, A 2017;696.
[33] Li Z, Wang Y, Cheng X, Li Z, Du J, Li S. The effect of Ti–Mo–Nb on the microstructures and tensile properties of a Fe–Mn–Al–C austenitic steel. Mater Sci Eng, A 2020;780.
[34] Brasche F, Haase C, Lipinska-Chwa M, Mayer J, Molodov DA. Combined κ-carbide precipitation and recovery enables ultra-high strength and ductility in light-weight steels. Mater Sci Eng, A 2020;795.
[35] Wei LL, Gao GH, Kim J, Misra RDK, Yang CG, et al. Ultrahigh strength-high ductility 1 GPa low density austenitic steel with ordered precipitation strengthening phase and dynamic slip band refinement. Mater Sci Eng, A 2022;838.
[36] Xie Z, Hui W, Zhang Y, Zhao X, Bai S. Achieving ultra-high yield strength in austenitic low-density steel via drastic VC precipitation. Mater Sci Eng, A 2022;861.
[37] Liu M, Li X, Zhang Y, Song C, Zhai Q. Multiphase precipitation and its strengthening mechanism in a V-containing austenite-based low density steel. Intermetallics 2021;134(107179).
[38] Welsch E, Ponge D, Hafez Haghighat SM, Sandlöbes S, Choi P, et al. Strain hardening by dynamic slip band refinement in a high-Mn lightweight steel. Acta Mater 2016;116.
[39] Thomason PF. A three-dimensional model for ductile fracture by the growth and coalescence of microvoids. Acta Mater 1985;33.
[40] Liu L, Yu Q, Wang Z, Ell J, Huang MX, Ritchie RO. Making ultrastrong steel tough by grain-boundary delamination. Science 2020;368.
[41] Choi WS, Cooman BCD, Sandlobes S, Raabem D. Size and orientation effects in partial dislocation-mediated deformation of twinning-induced plasticity steel micro-pillars. Acta Mater 2015;98.
[42] Li Y, Lu Y, Li W, Khedr M, Liu H, Jin X. Hierarchical microstructure design of a bimodal grained twinning induced plasticity steel with excellent cryogenic mechanical properties. Acta Mater 2018;158.
[43] Wang Z, Lu W, Zhao H, Liebscher CH, He J, Ponge D, et al. Ultrastrong lightweight compositionally complex steels via dual-nanoprecipitation. Sci Adv 2020;6.
[44] Su J, Raabe D, Li Z. Hierarchical microstructure design to tune the mechanical behavior of an interstitial TRIP-TWIP high-entropy alloy. Acta Mater 2019;163.
[45] Badiola DJ, Mendia AI, Gutiérrez I. Study by EBSD of the development of the substructure in a hot deformed 304 stainless steel. Mater Sci Eng, A 2005;394.
[46] Kim SD, park JY, park SJ, Jang Jh, Moon J, et al. Direct observation of dislocation plasticity in high-Mn lightweight steel by in-situ tem. Sci Rep 2019;9(15171).